LETTER

https://doi.org/10.1038/s41586-019-1497-4

Absence of a thick atmosphere on the terrestrial exoplanet LHS 3844b

Laura Kreidberg[1]*, Daniel D. B. Koll[2,13], Caroline Morley[3,13], Renyu Hu[4,5,13], Laura Schaefer[6], Drake Deming[7], Kevin B. Stevenson[8], Jason Dittmann[2], Andrew Vanderburg[3], David Berardo[9,10], Xueying Guo[9,10], Keivan Stassun[11], Ian Crossfield[9,10], David Charbonneau[1], David W. Latham[1], Abraham Loeb[1], George Ricker[9,10], Sara Seager[2,9,10,12] & Roland Vanderspek[9,10]

Most known terrestrial planets orbit small stars with radii less than 60 per cent of that of the Sun[1,2]. Theoretical models predict that these planets are more vulnerable to atmospheric loss than their counterparts orbiting Sun-like stars[3–6]. To determine whether a thick atmosphere has survived on a small planet, one approach is to search for signatures of atmospheric heat redistribution in its thermal phase curve[7–10]. Previous phase curve observations of the super-Earth 55 Cancri e (1.9 Earth radii) showed that its peak brightness is offset from the substellar point (latitude and longitude of 0 degrees)—possibly indicative of atmospheric circulation[11]. Here we report a phase curve measurement for the smaller, cooler exoplanet LHS 3844b, a 1.3-Earth-radii world in an 11-hour orbit around the small nearby star LHS 3844. The observed phase variation is symmetric and has a large amplitude, implying a dayside brightness temperature of 1,040 ± 40 kelvin and a nightside temperature consistent with zero kelvin (at one standard deviation). Thick atmospheres with surface pressures above 10 bar are ruled out by the data (at three standard deviations), and less-massive atmospheres are susceptible to erosion by stellar wind. The data are well fitted by a bare-rock model with a low Bond albedo (lower than 0.2 at two standard deviations). These results support theoretical predictions that hot terrestrial planets orbiting small stars may not retain substantial atmospheres.

We observed a light curve of the LHS 3844 system with the InfraRed Array Camera (IRAC)[12] of the Spitzer Space Telescope over 100 h between 4 February 2019 and 8 February 2019 (UT; Program 14204). We used IRAC's Channel 2 (a photometric bandpass over the wavelength range 4−5 μm) and read out the 32 × 32 pixel subarray using 2-s exposures. The observations began with a 30-min dithering sequence to allow the telescope to thermally settle. Following this pre-observation, we employed Spitzer's Pointing Calibration and Reference Sensor (PCRS) 'peak-up' mode to position the target on the detector's 'sweet spot'—a pixel with minimal variation in sensitivity. After the first 60 h of observation, there was a 3-h break for data downlink. The data collection recommenced with another 30-min thermal settling period and continued in PCRS peak-up mode for 40 h. The telescope was repointed every 20 h to keep the image centred on the detector's sweet spot.

We began our analysis with the Basic Calibrated Data product provided by the Spitzer Science Center pipeline and reduced it with a custom aperture photometry routine[13]. This routine upsampled each exposure by a factor of 5 in the X and Y dimensions and fitted a two-dimensional Gaussian profile to determine the image centre. We estimated the background from the median value in an annulus 7 to 15 pixels from the target centre. Bad pixels were identified and masked using iterative outlier clipping over groups of 64 exposures. We then summed the flux in a fixed aperture centred on the target. We varied the aperture size from 2 to 4 pixels in 0.5-pixel increments and selected a 2.5-pixel aperture to minimize noise in the resulting light curve.

We fitted the extracted light curve with a simultaneous model of the astrophysical signal and the instrument behaviour. The astrophysical signal consisted of a transit model and a first-degree spherical-harmonics temperature map to represent the planet's thermal phase variation[14,15]. The instrument model had two components: a two-dimensional spline fitted to Spitzer's pixel sensitivity variations and a linear scaling with the half-width of the point spread function in both the X and Y directions[16,17]. We determined the best-fit model parameters with a least-squares minimization routine and estimated uncertainties with differential-evolution Markov chain Monte Carlo (MCMC) analysis. We explored alternative models for both the instrument systematics and the planet's thermal phase variation and obtained consistent results with our nominal model (see Methods for further details).

Figure 1 shows the measured thermal phase curve and best-fit temperature map. The secondary-eclipse depth is 380 ± 40 p.p.m. and the peak-to-trough amplitude of the phase variation is 350 ± 40 p.p.m. The values correspond to a dayside brightness temperature of 1,040 ± 40 K and a nightside brightness temperature that is broadly consistent with zero (0–710 K; all uncertainties are 1σ unless otherwise specified). The longitude of peak brightness is consistent with zero degrees (−6° ± 6°). The inferred planet-to-star radius ratio is $R_p/R_s = 0.0641 \pm 0.0003$, which is consistent with the ratio of the corresponding optical-wavelength radii[18]. The secondary-eclipse time agrees with expectations for a zero-eccentricity orbit. We find no evidence for transit time variations (the transit times deviate from a linear ephemeris at 0.1σ confidence). From a joint fit to the Spitzer and TESS (Transiting Exoplanet Survey Satellite) transit times, we revise the time of central transit to 2458325.22559 ± 0.00025 (barycentric Julian date in the barycentric dynamical time system), and the orbital period to 0.4629279 ± 0.0000006 d. We also establish upper limits for transits of other planets in this system, using a joint fit to the TESS and Spitzer data. In the orbital period range 0.5–6 d, our 3σ upper limit corresponds to $0.6R_\oplus$ ($R_\oplus$, Earth radius) and in 6–12 d our 3σ upper limit is $0.8R_\oplus$.

The phase curve is consistent with expectations for a synchronously rotating bare rock—a completely absorptive surface in instantaneous thermal equilibrium that radiates isotropically (Extended Data Fig. 1). In this simple picture, the amplitude of the phase curve requires the surface to be very absorptive, with an upper limit on the Bond albedo of 0.2 at 2σ confidence. We model the emission spectra of several rocky surfaces[19] and compare them with the measured planet-to-star flux

[1]Center for Astrophysics | Harvard & Smithsonian, Cambridge, MA, USA. [2]Department of Earth, Atmospheric and Planetary Sciences, Massachusetts Institute of Technology, Cambridge, MA, USA. [3]Department of Astronomy, The University of Texas at Austin, Austin, TX, USA. [4]Jet Propulsion Laboratory, California Institute of Technology, Pasadena, CA, USA. [5]Division of Geological and Planetary Sciences, California Institute of Technology, Pasadena, CA, USA. [6]Geological Sciences Department, Stanford University, Stanford, CA, USA. [7]Department of Astronomy, University of Maryland, College Park, MD, USA. [8]Space Telescope Science Institute, Baltimore, MD, USA. [9]Department of Physics, Massachusetts Institute of Technology, Cambridge, MA, USA. [10]Kavli Institute for Astrophysics and Space Research, Massachusetts Institute of Technology, Cambridge, MA, USA. [11]Department of Physics and Astronomy, Vanderbilt University, Nashville, TN, USA. [12]Department of Aeronautics and Astronautics, Massachusetts Institute of Technology, Cambridge, MA, USA. [13]These authors contributed equally: Daniel D. B. Koll, Caroline Morley, Renyu Hu.
*e-mail: laura.kreidberg@cfa.harvard.edu

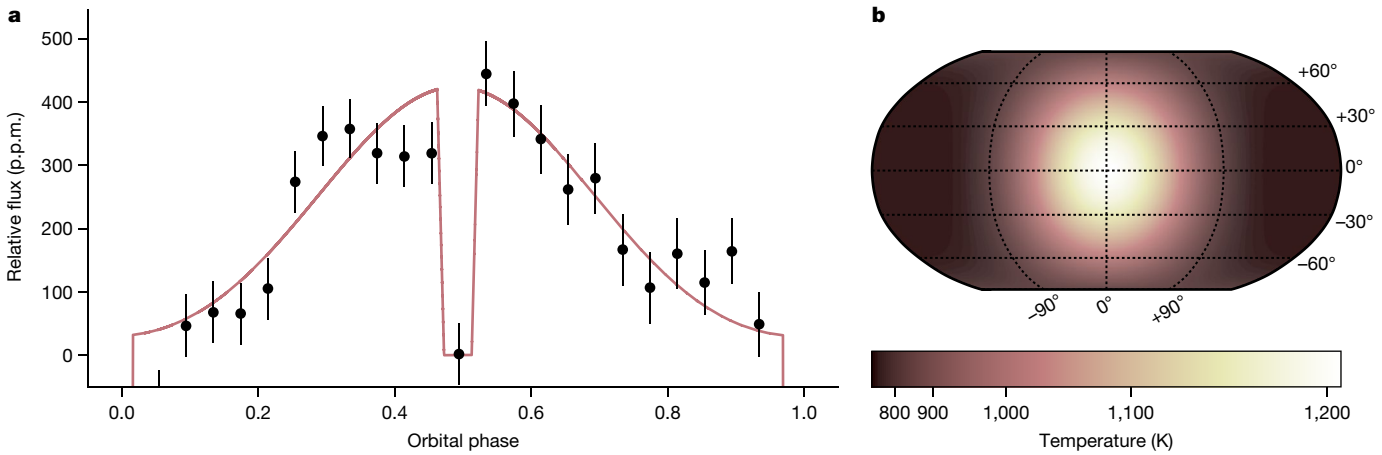

Fig. 1 | 4.5-μm thermal phase curve of LHS 3844b and best-fit temperature map. a, Planet-to-star flux binned over 25 equally spaced intervals over the planet's 11.1-h orbital period (points with 1σ uncertainties) compared to the best-fit phase curve (line). The data are normalized so that the relative flux is zero when the planet is eclipsed by the star at orbital phase 0.5. **b**, Spherical-harmonics temperature map used to generate the phase variation model. The planet's substellar point corresponds to latitude and longitude of (0°, 0°). We note that the spherical-harmonics model includes north–south temperature variation, but only east–west variation is constrained by the data.

(Fig. 2). We consider multiple geologically plausible planetary surface types, including primary crusts that form from solidification of a magma ocean (ultramafic and feldspathic), secondary crust that forms from volcanic eruptions (basaltic) and a tertiary crust that forms from tectonic re-processing (granitoid). Governed by the reflectivity in the visible and the near-infrared and the emissivity in the mid-infrared, these surface types have distinct emission spectra. The measured planet-to-star flux for LHS 3844b is most consistent with a basaltic composition. Such a surface is comparable to the lunar mare and Mercury, and could result from widespread extrusive volcanism[20]. Pure feldspathic and granitoid compositions provide a poor fit to the data and must be mixed with a surface at least 40% basaltic or 75% ultramafic to to be consistent with the measured eclipse depth at 3σ.

We also explore the possibility that the planet has an atmosphere. We develop a simple model to account for both the atmospheric heat redistribution and absorption features from plausible chemical compositions. We parameterize the day–night atmospheric heat redistribution with a scaling that is based on analytic theory[10] and that accounts for the dynamical effects of the surface pressure, p_s, and the atmospheric optical thickness, τ_{LW} (see Methods for the equation and a validation of the scaling against dynamical models). To estimate the planet's eclipse depth in the Spitzer 4.5-μm bandpass, we construct one-dimensional radiative-transfer models[21] tuned to match the heat redistribution scaling. Motivated by the atmospheric evolution models of hot, terrestrial planets[22–24], we consider model atmospheric compositions that are mixtures of oxygen (O_2) and carbon dioxide (CO_2) over a range of surface pressures of 0.001−100 bar (1 bar = 10^5 Pa). We also consider nitrogen (N_2) mixtures with trace carbon dioxide.

Figure 3 shows the predicted eclipse depths for the O_2/CO_2 models compared to the measured values. Higher surface pressures correspond to smaller eclipse depths (implying a cooler dayside) because thick atmospheres are more efficient at transporting energy to the planet's nightside. Higher CO_2 abundances also decrease the predicted eclipse depths, owing to strong absorption by CO_2 in the Spitzer 4.5-μm bandpass that pushes the photosphere to higher, cooler layers. Overall, we find that the best-fit models have surface pressures below 0.1 bar. Carbon dioxide-dominated atmospheres are ruled out for surface pressures as low as that of Mars (0.006 bar), and surface pressures above 10 bar are ruled out for all compositions that we consider (greater than 3σ confidence). For N_2 mixtures, high surface pressures are ruled out at even higher confidence (for example, a 10-bar N_2 atmosphere with 1 p.p.m. CO_2 is excluded at 6σ).

As an independent test of these results, we also fit the measured phase curve variation with an energy balance model that computes reflection, longitudinal heat redistribution and thermal emission. The model is parameterized by the planet's Bond albedo, the ratio of radiative to advective timescales and a greenhouse-warming factor[25,26]. For photometric data like ours, the Bond albedo and greenhouse factor are degenerate, but we include both parameters to capture the possibility that the observed brightness temperature is different from the energy balance temperature. On the basis of an MCMC analysis, we infer a value of $\tau_{rad}/\tau_{adv} < 0.3$ at 2σ confidence. For a typical wind speed of 300 m s^{-1} for atmospheres with high mean molecular weight[27,28], and assuming a surface gravity of 16 m s^{-2}, consistent with an Earth-like bulk composition (the planet's mass is not yet known), this requirement implies a photospheric pressure lower than 0.06 bar, in agreement with our finding that the data are fitted well by tenuous O_2- and N_2-dominated atmospheres with trace amounts of CO_2.

To explore whether a tenuous atmosphere or no atmosphere at all is more likely for LHS 3844b, we model atmospheric escape over the planet's lifetime[24]. The initial atmosphere is assumed to be pure water, which can either dissolve within a magma ocean formed by accretion-induced heating during planet formation or photolyse into hydrogen and oxygen owing to high-energy stellar radiation in the extreme ultraviolet

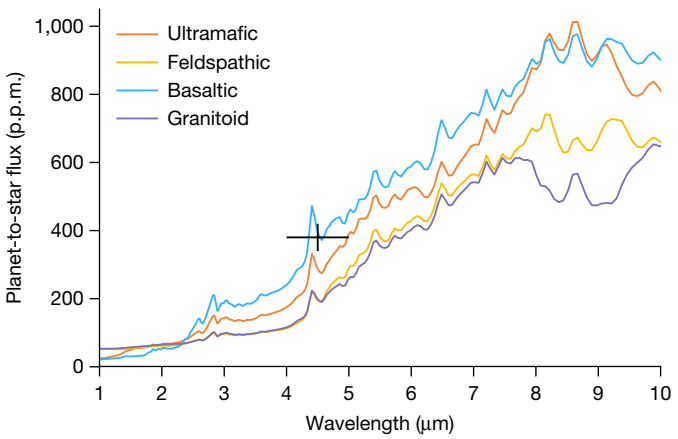

Fig. 2 | Predicted emission spectrum for a range of surface compositions. The measured planet-to-star flux is shown in black, with vertical error bars denoting the 1σ confidence interval and horizontal error bars denoting the width of the Spitzer photometric bandpass. The value is most consistent with a pure dark-basaltic surface. Mixed surface compositions require at least 40% basalt or 75% ultramafic rock to be consistent with the data at 3σ confidence.

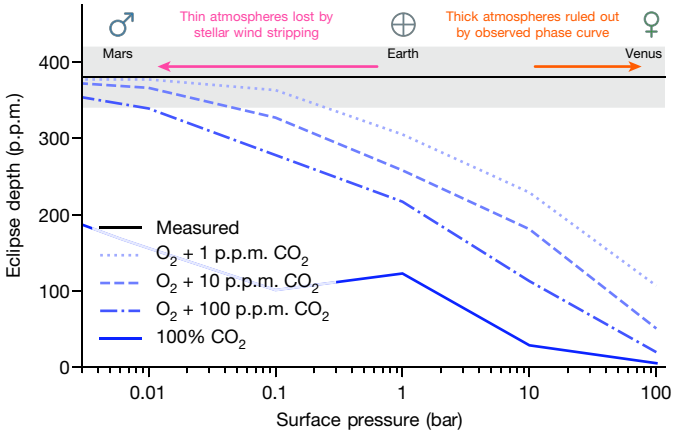

Fig. 3 | Predicted 4.5-μm eclipse depths for model atmospheres compared to the measured value. The grey region represents the 1σ uncertainty on the measured eclipse depth. The model atmospheres are composed of oxygen–carbon dioxide mixtures and account for heat transport to the planet's nightside. We indicate the surface pressures of Mars, Earth and Venus with grey symbols. The orange arrow indicates surface pressures that are inconsistent with the observed eclipse depth ($>3\sigma$ confidence); the pink arrow shows surfaces pressures that are susceptible to erosion by stellar wind.

(XUV) wavelength range[29] (0.1–100 nm). Most of the atomic hydrogen and oxygen escape to space, but some remnant oxygen reacts with the magma ocean or remains in the atmosphere as O_2. We assume that the early XUV flux is a constant fraction of the stellar bolometric luminosity (the 'saturation fraction') until the star is 1 Gyr old and then decays with time following a power law[4,29]. In our model, we vary both the initial planetary water abundance and the XUV saturation fraction. Figure 4 shows the resulting surface pressures compared to the 3σ upper limit of 10 bar obtained in this work. For a typical saturation fraction for low-mass stars[30], we find that the initial planetary water

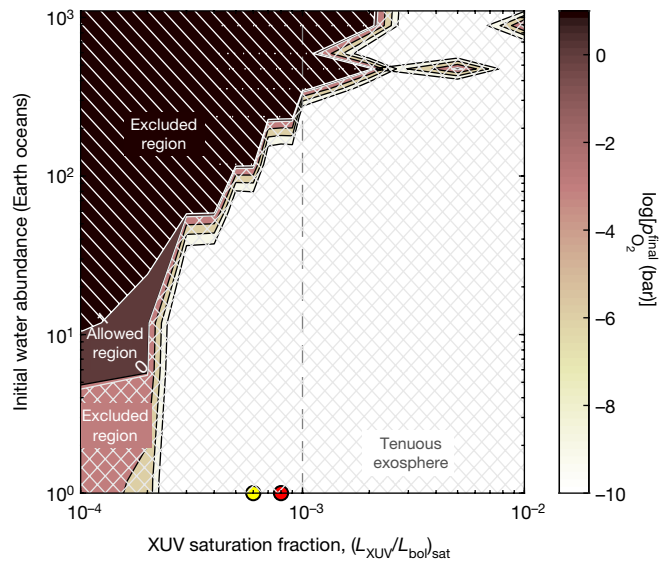

Fig. 4 | Final atmospheric pressure after 5 Gyr of energy-limited atmospheric escape. The contours indicate final surface pressure as a function of the XUV saturation fraction and the initial water abundance. Labels '0' and '1' indicate $\log(p_{O_2}^{final}) = 0$ and $\log(p_{O_2}^{final}) = 1$—the allowed range from our data. For all cases considered here all water is lost by the end of the simulation, but residual O_2 gas remains. Present-day surface pressures greater than 10 bar (single-hatched region) are excluded on the basis of the observed phase curve amplitude, and pressures below 0.7 bar are susceptible to erosion by stellar wind (cross-hatched region). The vertical dashed line marks the nominal saturation fraction for LHS 3844. The yellow and red dots on the horizontal axis show the L_{XUV}/L_{bol} of the early Sun and a young M-dwarf (AD Leo), respectively[29,30].

abundance could not exceed 240 Earth oceans. For lower initial water abundances or higher XUV saturation, the atmosphere is entirely lost. Further, we estimate that an atmosphere of 1–10 bar could be eroded by stellar winds (see Methods for details). Given that thick atmospheres are ruled out by the data and thin atmospheres are unstable over the planet's lifetime, LHS 3844b is probably a bare rock, unless a thin atmosphere is continually replenished over time.

The results presented here motivate similar studies for less-irradiated planets orbiting small stars. Cooler planets are less susceptible to atmospheric escape and erosion, and may provide a friendlier environment for the evolution of life. In coming years this hypothesis can be tested using the infrared-wavelength coverage of the James Webb Space Telescope and the influx of planet detections expected from current and future surveys.

Online content

Any methods, additional references, Nature Research reporting summaries, source data, extended data, supplementary information, acknowledgements, peer review information; details of author contributions and competing interests; and statements of data and code availability are available at https://doi.org/10.1038/s41586-019-1497-4.

Received: 22 March 2019; Accepted: 22 July 2019;
Published online 19 August 2019.

1. Dressing, C. D. & Charbonneau, D. The occurrence of potentially habitable planets orbiting M dwarfs estimated from the full Kepler dataset and an empirical measurement of the detection sensitivity. *Astrophys. J.* **807**, 45 (2015).
2. Fulton, B. J. et al. The California–Kepler survey. III. A gap in the radius distribution of small planets. *Astron. J.* **154**, 109 (2017).
3. Tarter, J. C. et al. A reappraisal of the habitability of planets around M-dwarf stars. *Astrobiology* **7**, 30–65 (2007).
4. Luger, R. & Barnes, R. Extreme water loss and abiotic O_2 buildup on planets throughout the habitable zones of M dwarfs. *Astrobiology* **15**, 119–143 (2015).
5. Wordsworth, R. Atmospheric heat redistribution and collapse on tidally locked rocky planets. *Astrophys. J.* **806**, 180 (2015).
6. Shields, A. L., Ballard, S. & Johnson, J. A. The habitability of planets orbiting M-dwarf stars. *Phys. Rep.* **663**, 1–38 (2016).
7. Seager, S. & Deming, D. On the method to infer an atmosphere on a tidally locked super Earth exoplanet and upper limits to GJ 876d. *Astrophys. J.* **703**, 1884–1889 (2009).
8. Selsis, F., Wordsworth, R. D. & Forget, F. Thermal phase curves of nontransiting terrestrial exoplanets. I. Characterizing atmospheres. *Astron. Astrophys.* **532**, A1 (2011).
9. Kreidberg, L. & Loeb, A. Prospects for characterizing the atmosphere of Proxima Centauri b. *Astrophys. J. Lett.* **832**, 12 (2016).
10. Koll, D. D. B. & Abbot, D. S. Temperature structure and atmospheric circulation of dry tidally locked rocky exoplanets. *Astrophys. J.* **825**, 99 (2016).
11. Demory, B.-O. et al. A map of the large day–night temperature gradient of a super-Earth exoplanet. *Nature* **532**, 207–209 (2016).
12. Fazio, G. G. et al. The Infrared Array Camera (IRAC) for the Spitzer Space Telescope. *Astrophys. J. Suppl. Ser.* **154**, 10–17 (2004).
13. Cubillos, P. et al. WASP-8b: characterization of a cool and eccentric exoplanet with Spitzer. *Astrophys. J.* **768**, 42 (2013).
14. Kreidberg, L. batman: BAsic Transit Model cAlculatioN in Python. *Publ. Astron. Soc. Pac.* **127**, 1161–1165 (2015).
15. Louden, T. & Kreidberg, L. SPIDERMAN: an open-source code to model phase curves and secondary eclipses. *Mon. Not. R. Astron. Soc.* **477**, 2613–2627 (2018).
16. Stevenson, K. B. et al. Transit and eclipse analyses of the exoplanet HD 149026b using BLISS mapping. *Astrophys. J.* **754**, 136 (2012).
17. Lanotte, A. A. et al. A global analysis of Spitzer and new HARPS data confirms the loneliness and metal-richness of GJ 436 b. *Astron. Astrophys.* **572**, A73 (2014).
18. Vanderspek, R. et al. TESS discovery of an ultra-short-period planet around the nearby M dwarf LHS 3844. *Astrophys. J. Lett.* **871**, 24 (2019).
19. Hu, R., Ehlmann, B. L. & Seager, S. Theoretical spectra of terrestrial exoplanet surfaces. *Astrophys. J.* **752**, 7 (2012).
20. de Pater, I. & Lissauer, J. *Planetary Sciences* (Cambridge Univ. Press, 2001).
21. Morley, C. V., Kreidberg, L., Rustamkulov, Z., Robinson, T. & Fortney, J. J. Observing the atmospheres of known temperate Earth-sized planets with JWST. *Astrophys. J.* **850**, 121 (2017).
22. Wordsworth, R. D. & Pierrehumbert, R. T. Water loss from terrestrial planets with CO_2-rich atmospheres. *Astrophys. J.* **778**, 154 (2013).
23. Wordsworth, R. & Pierrehumbert, R. Abiotic oxygen-dominated atmospheres on terrestrial habitable zone planets. *Astrophys. J. Lett.* **785**, 20 (2014).
24. Schaefer, L., Wordsworth, R. D., Berta-Thompson, Z. & Sasselov, D. Predictions of the atmospheric composition of GJ 1132b. *Astrophys. J.* **829**, 63 (2016).

25. Hu, R., Demory, B.-O., Seager, S., Lewis, N. & Showman, A. P. A semi-analytical model of visible-wavelength phase curves of exoplanets and applications to Kepler-7 b and Kepler-10 b. *Astrophys. J.* **802**, 51 (2015).
26. Angelo, I. & Hu, R. A case for an atmosphere on super-Earth 55 Cancri e. *Astron. J.* **154**, 232 (2017).
27. Kataria, T., Showman, A. P., Fortney, J. J., Marley, M. S. & Freedman, R. S. The atmospheric circulation of the super Earth GJ 1214b: dependence on composition and metallicity. *Astrophys. J.* **785**, 92 (2014).
28. Zhang, X. & Showman, A. P. Effects of bulk composition on the atmospheric dynamics on close-in exoplanets. *Astrophys. J.* **836**, 73 (2017).
29. Ribas, I. et al. First determination of the distance and fundamental properties of an eclipsing binary in the Andromeda galaxy. *Astrophys. J. Lett.* **635**, 37–40 (2005).
30. Chadney, J. M., Galand, M., Unruh, Y. C., Koskinen, T. T. & Sanz-Forcada, J. XUV-driven mass loss from extrasolar giant planets orbiting active stars. *Icarus* **250**, 357–367 (2015).

METHODS

Data analysis. In this section we provide additional description of the data analysis. Our nominal model for the planet's phase variation was a first-degree spherical-harmonics temperature map for the planet. For each point in the time series, we computed the planet-to-star flux ratio for the viewing geometry at that time[15]. We multiplied the planet-to-star flux by a transit model to account for the drop in stellar flux when the planet obscures the star.

We used a differential-evolution MCMC algorithm to obtain the posterior distribution of the model parameters[31]. The free parameters for the fit were the planet-to-star radius ratio, the time of central transit, a linear limb-darkening parameter and four coefficients for the spherical-harmonics model. The fit also had free parameters for a normalization constant and linear scaling of the pixel response function (PRF) width in both the X and Y directions[17]. We fixed the other orbital parameters on the best-fit values from the discovery paper[18]. We initially allowed the secondary-eclipse time to vary but found that it was consistent with expectations for zero eccentricity, so our final fit assumed a circular orbit. We also applied a prior that assigned zero probability to solutions with temperature maps that dropped below zero.

Over the observation, the telescope was repointed several times (see Extended Data Fig. 2). We assumed that the astrophysical parameters were the same for all five pointings but allowed the systematics parameters to vary. We fitted all the data simultaneously. We masked two short segments of data that showed correlated noise in the residuals (grey shading in Extended Data Fig. 2). As a test of the fit quality, we made an Allan deviation plot (Extended Data Fig. 3). The root-mean-square deviation decreases as the square root of the number of data points per bin, as expected for photon noise-limited statistics. We rescaled the estimated uncertainty per data point by a factor of 1.07 to achieve a reduced χ^2 value of unity for the best fit. We then ran the differential-evolution MCMC algorithm with four chains until the Gelman–Rubin statistic dropped below 1.01.

In addition to the spherical-harmonics model, we also tested a sinusoid model, which has been commonly used to fit other phase curve data[11]. The only reason that the two models would produce different phase curves is that the transformation from temperature to flux (the Planck function) is not linear. The sinusoid peak-to-trough amplitude was 402 ± 46 p.p.m., the eclipse depth as 425 ± 54 p.p.m. and the longitude of peak brightness is consistent with the substellar point ($-3.0° \pm 6.0°$). The phase curve amplitude and eclipse depth are consistent within 1σ with the results from the spherical-harmonics model. We inverted the sinusoid to estimate the planet's temperature as a function of longitude[32] and found that the nightside temperature was below zero for the best-fit sinusoid. Similar behaviour has been observed for other phase curves with large amplitudes, and in general can be remedied by the addition of odd harmonics in the sinusoid model[33]. In this work, we focus on the spherical-harmonics fit, where we impose positive nightside temperatures.

Effects of red noise. For the main analysis reported in this paper, we trimmed small sections of data that exhibited time-correlated noise (Extended Data Fig. 2). As a test, we also performed a full MCMC fit to the entire dataset, accounting for red noise on the timescale of the eclipse duration[34]. For the full dataset, we obtained an eclipse depth and sine curve amplitude of 490 ± 70 p.p.m. and 450 ± 70 p.p.m., respectively. These results are consistent with the values reported for the trimmed data and do not change the conclusions of the paper.

Independent data reduction and analysis. We checked our results using an independent analysis with first-order pixel-level decorrelation (PLD)[35]. First-order PLD has limited applications to phase curves because the image motion can exceed the limits of the first-order approximation. Therefore our PLD analysis focused on checking the amplitudes of the transit and secondary eclipse. We fitted the eclipse and transit separately, each with a range in orbital phase that is as large as possible (adjusted by trial and error) while still preserving the highest possible precision in the fits. We reduced red noise by fitting to binned data[35]. Our PLD code selected the optimum bin size and the optimum radius of the photometric aperture on the basis of minimizing the χ^2 value in a fit to the Allan deviation curve[36]. For the eclipse, we binned the data by 392 points, versus a 189-point binning for the transit. For the modelled eclipse and transit curves we used the same binning as for the data to avoid bias in the fits, and we verified that the derived transit and eclipse amplitudes do not vary systematically with the bin size.

Because the orbital ephemeris has been determined recently and precisely from TESS observations[18], we fixed the phase of transit to 0.0 and the phase of secondary eclipse to 0.5. We used quadratic limb darkening for the transit[37]. Because infrared limb darkening is small, we also fixed those coefficients during the transit fitting process. The PLD code determined the best-fit transit and eclipse amplitudes using multivariate linear regression and then estimated the uncertainties with MCMC. The independent variables in the fit were the 12 basis pixels[36], a linear ramp in time and the modelled transit/eclipse curve. The MCMC analysis consisted of a 50,000-step burn-in segment, followed by a 500,000-step chain using Metropolis–Hastings sampling. We ran independent chains to verify convergence. The posterior distributions for eclipse and transit amplitude are nearly Gaussian, and centred on the best-fit values from the multivariate regression. Because the derived amplitudes vary stochastically with different bin sizes, we included that effect in the amplitude errors by repeating the regressions over a range of bin sizes that give acceptable fits. We added the dispersion in amplitudes obtained from that process in quadrature with the uncertainty from the MCMC analysis to arrive at total error bars for the results (the MCMC uncertainties dominate).

Our best fits for the transit and eclipse are illustrated in Extended Data Fig. 4. Our secondary-eclipse amplitude from the PLD fits is 439 ± 54 p.p.m., which differs from the nominal value that we obtained from the phase curve analysis (380 ± 40 p.p.m.) by 0.9σ . The brightness of the star in the infrared and the small limb darkening facilitate a precise radius measurement from the Spitzer transits. We find $R_p/R_s = 0.0641 \pm 0.0003$, in excellent agreement with the ratio of the optical-wavelength radii[18], $R_p/R_s = 0.0635 \pm 0.0009$.

As a test, we also attempted a PLD fit to the entire phase curve. For this analysis, we modified the PLD technique by adding quadratic terms for each pixel while neglecting cross-terms[28]. We selected a 5×5 pixel aperture centred on star LHS 3844, from which we extracted our light curve. In addition to the coefficients for each pixel, we also adopted a quadratic function in time to correct for the long term drift in photometry. Each astronomical observation request was reduced independently. Prior to fitting the data, we rejected all data points more than 10 median absolute deviations away from a 1-h-wide sliding median to eliminate the effect of large outliers in our data. Before fitting our phase curve, we eliminated all data points that occurred during the primary transit of LHS 3844b and those that occurred within 1 transit duration to avoid biasing our result. We found that the PLD reduction produces consistent results with our primary analysis: the best-fit sinusoidal model had a peak-to-trough phase curve amplitude of 310 p.p.m. and a secondary-eclipse depth of 335 p.p.m. However, the fit had time-correlated noise that made it challenging to robustly estimate uncertainties. For these data, the target centroid motion is large enough to ensure that the assumptions behind PLD break down, and the results from the two-dimensional-spline mapping technique[16] are more robust.

Spectral energy distribution fit. The theoretical models in this paper require an estimate of the stellar spectrum. We estimated the spectrum with a spectral energy distribution fit using all available photometry. The fit (shown in Extended Data Fig. 5) gave a metallicity of $[\mathrm{Fe}]/[\mathrm{H}] = 0.0^{+0.0}_{-1.0}$ and a bolometric luminosity of $F_{\mathrm{bol}} = 3.52 \pm 0.33$ erg s^{-1} cm^{-2} (measured at Earth). From these values and the Gaia parallax[38], we derived a stellar radius of $R_* = 0.178 R_\odot \pm 0.012 R_\odot$ ($R_\odot$, solar radius; assuming a stellar effective temperature of $T_{\mathrm{eff}} = 3036 \pm 77$ K)[18] and a stellar mass of $M_* = 0.158 M_\odot \pm 0.004 M_\odot$. ($M_\odot$, mass of the Sun)[39]. There is chromospheric emission in the GALEX (Galaxy Evolution Explorer) far-ultraviolet band that could contribute to present-day photoevaporation of the planetary atmosphere.

Model for atmospheric heat redistribution. We computed the planet's broadband dayside-averaged brightness temperature using the following scaling:

$$T_{\mathrm{day}} = T_* \sqrt{\frac{R_*}{d}} (1 - \alpha_{\mathrm{B}})^{1/4} f^{1/4} \tag{1}$$

where

$$f = \frac{2}{3} - \frac{5}{12} \times \frac{\tau_{\mathrm{LW}} \left(\frac{p_s}{1\,\mathrm{bar}}\right)^{2/3} \left(\frac{T_{\mathrm{eq}}}{600\,\mathrm{K}}\right)^{-4/3}}{2 + \tau_{\mathrm{LW}} \left(\frac{p_s}{1\,\mathrm{bar}}\right)^{2/3} \left(\frac{T_{\mathrm{eq}}}{600\,\mathrm{K}}\right)^{-4/3}} \tag{2}$$

Here T_* is the stellar effective temperature, R_* is the stellar radius, d is the semi-major axis, α_{B} is the planetary albedo and T_{eq} is the planet's equilibrium temperature. The derivation for the scaling will be presented elsewhere (Koll et al.[40]). To validate the scaling, Extended Data Fig. 6 compares the dayside eclipse depths predicted by the scaling against the dayside eclipses simulated with a general circulation model (GCM) with tidally locked orbital parameters and semi-grey radiative transfer. The scaling successfully captures the main variation in the GCM's day–night heat redistribution.

To include our scaling in the one-dimensional radiative-transfer model, we calculated the broadband optical thickness τ_{LW} for a given atmospheric composition and surface pressure using the atmosphere's attenuation of the surface's thermal emission,

$$\tau_{\mathrm{LW}} = -\ln\left(\frac{\int \mathrm{e}^{-\tau_\lambda} B_\lambda(T_s)\,\mathrm{d}\lambda}{\int B_\lambda(T_s)\,\mathrm{d}\lambda}\right) \tag{3}$$

Here B_λ is the Planck function, T_s is the surface temperature and τ_λ is the atmosphere's column-integrated optical thickness at a given wavelength λ, computed with the one-dimensional radiative-transfer model.

Atmospheric escape due to stellar wind. Interaction with a stellar wind can also be a considerable source of atmospheric erosion. We estimated the erosion for LHS 3844b on the basis of ion escape rates of 10^{26}–10^{27} s^{-1} (equivalent to a mass loss of 3–30 kg s^{-1}; ref. [41]) calculated for Proxima Centauri b. Proxima Centauri has approximately the same stellar type as that of LHS 3844. When scaling for orbital distance, the stellar wind flux onto LHS 3844b is about 10 times larger than for Proxima Centauri b, corresponding to a mass loss rate of 30–300 kg s^{-1}. Assuming a constant stellar wind flux over the planet's lifetime, this implies a total mass loss of 10^{18}–10^{19} kg, equivalent to 0.7–7 bar. The stellar wind flux was probably higher during the star's active period, so this value is a lower limit to the amount of escape that could be driven by the stellar wind alone.

Stability to atmospheric collapse. We explored the possibility of atmospheric collapse by comparing LHS 3844b to previously published models of synchronously rotating planets with CO_2-dominated atmospheres[5]. In the simulations, planets with three times the insolation of Earth ($S_\oplus$) were stable to collapse for surface pressures of 0.03 bar (assuming $M_P = 1M_\oplus$; $M_\oplus$, mass of Earth) or 0.4 bar ($10M_\oplus$). The higher the insolation is, the more stable the atmosphere is to collapse. Because LHS 3844b is much more highly irradiated than the range of planets considered ($70S_\oplus$), we expect that surface pressures below about 0.1 bar are stable. In the non-synchronous case the planet is more evenly heated, making atmospheric collapse even less likely.

Data availability

The raw data used in this study are available at the Spitzer Heritage Archive, https://sha.ipac.caltech.edu/applications/Spitzer/SHA.

Code availability

We processed and fitted the data with the open-source pipeline POET, which is available at https://github.com/kevin218/POET. We used the code version corresponding to commit ID adbe62e7b733df9541231e8d1e5d32b7e2cdad76.

31. Braak, C. J. F. T. A Markov chain Monte Carlo version of the genetic algorithm differential evolution: easy Bayesian computing for real parameter spaces. *Stat. Comput.* **16**, 239–249 (2006).
32. Cowan, N. B. & Agol, E. Inverting phase functions to map exoplanets. *Astrophys. J. Lett.* **678**, 129 (2008).
33. Keating, D. & Cowan, N. B. Revisiting the energy budget of WASP-43b: enhanced day–night heat transport. *Astrophys. J. Lett.* **849**, 5 (2017).
34. Pont, F., Zucker, S. & Queloz, D. The effect of red noise on planetary transit detection. *Mon. Not. R. Astron. Soc.* **373**, 231–242 (2006).
35. Deming, D. et al. Spitzer secondary eclipses of the dense, modestly-irradiated, giant exoplanet HAT-P-20b using pixel-level decorrelation. *Astrophys. J.* **805**, 132 (2015).
36. Garhart, E. et al. Statistical characterization of hot Jupiter atmospheres using Spitzer's secondary eclipses. Preprint at https://arxiv.org/abs/1901.07040 (2019).
37. Claret, A., Hauschildt, P. H. & Witte, S. New limb-darkening coefficients for PHOENIX/1D model atmospheres. I. Calculations for 1500 K $\leq T_{\rm eff} \leq$ 4800 K Kepler, CoRot, Spitzer, uvby, UBVRIJHK, Sloan, and 2MASS photometric systems. *Astron. Astrophys.* **546**, A14 (2012).
38. Gaia Collaboration. Gaia Data Release 2. Summary of the contents and survey properties. *Astron. Astrophys.* **616**, A1 (2018).
39. Mann, A. W. et al. How to constrain your M dwarf. II. The mass–luminosity–metallicity relation from 0.075 to 0.70 solar masses. *Astrophys. J.* **871**, 63 (2019).
40. Koll, D. D. B. A scaling theory for atmospheric heat redistribution on rocky exoplanets. Preprint at https://arxiv.org/abs/1907.13145 (2019).
41. Dong, C., Lingam, M., Ma, Y. & Cohen, O. Is Proxima Centauri b habitable? A study of atmospheric loss. *Astrophys. J. Lett.* **837**, 26 (2017).
42. Frierson, D. M. W., Held, I. M. & Zurita-Gotor, P. A gray-radiation aquaplanet moist GCM. Part I: static stability and eddy scale. *J. Atmos. Sci.* **63**, 2548–2566 (2006).
43. Merlis, T. M. & Schneider, T. Atmospheric dynamics of Earth-like tidally locked aquaplanets. *J. Adv. Model. Earth Syst.* **2**, 13 (2010).
44. Koll, D. D. B. & Abbot, D. S. Deciphering thermal phase curves of dry, tidally locked terrestrial planets. *Astrophys. J.* **802**, 21 (2015).

Acknowledgements L.K. is a Junior Fellow of the Harvard Society of Fellows. J.D. is a 51 Pegasi b Postdoctoral Fellow. A.V. is a NASA Sagan Fellow. D.D.B.K. was supported by a James S. McDonnell Foundation postdoctoral fellowship. R.H. is supported in part by NASA Grant number 80NM0018F0612. The research was carried out at the Jet Propulsion Laboratory, California Institute of Technology, under a contract with the National Aeronautics and Space Administration. A.V.'s work was performed under contract with the California Institute of Technology (Caltech)/Jet Propulsion Laboratory, funded by NASA through the Sagan Fellowship Program executed by the NASA Exoplanet Science Institute. D.C. acknowledges support from the John Templeton Foundation. The opinions expressed in this publication are those of the authors and do not necessarily reflect the views of the John Templeton Foundation.

Author contributions L.K. conceived the project, planned the observations and carried out the primary data reduction. D.D.B.K., C.M. and R.H. ran theoretical models for the planet's atmosphere and surface. L.S. provided atmospheric evolution models. D.D., K.B.S., J.D., A.V., D.B. and X.G. contributed to the data analysis. K.S. modelled the stellar spectrum. I.C., D.C., D.W.L., A.L., G.R., S.S. and R.V. provided useful comments on the manuscript and assisted with the observing proposal.

Competing interests The authors declare no competing interests.

Additional information
Correspondence and requests for materials should be addressed to L.K.
Peer review information *Nature* thanks Nicolas Cowan and the other, anonymous, reviewer(s) for their contribution to the peer review of this work.
Reprints and permissions information is available at http://www.nature.com/reprints.

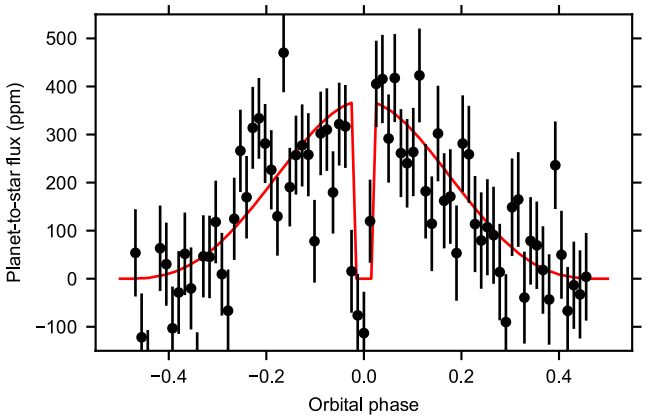

Extended Data Fig. 1 | LHS 3844b phase curve compared to predictions for a bare rock. The model (red line) assumes that the incident stellar flux is totally absorbed (zero Bond albedo) and is reradiated instantaneously and isotropically. The error bars correspond to 1σ uncertainties.

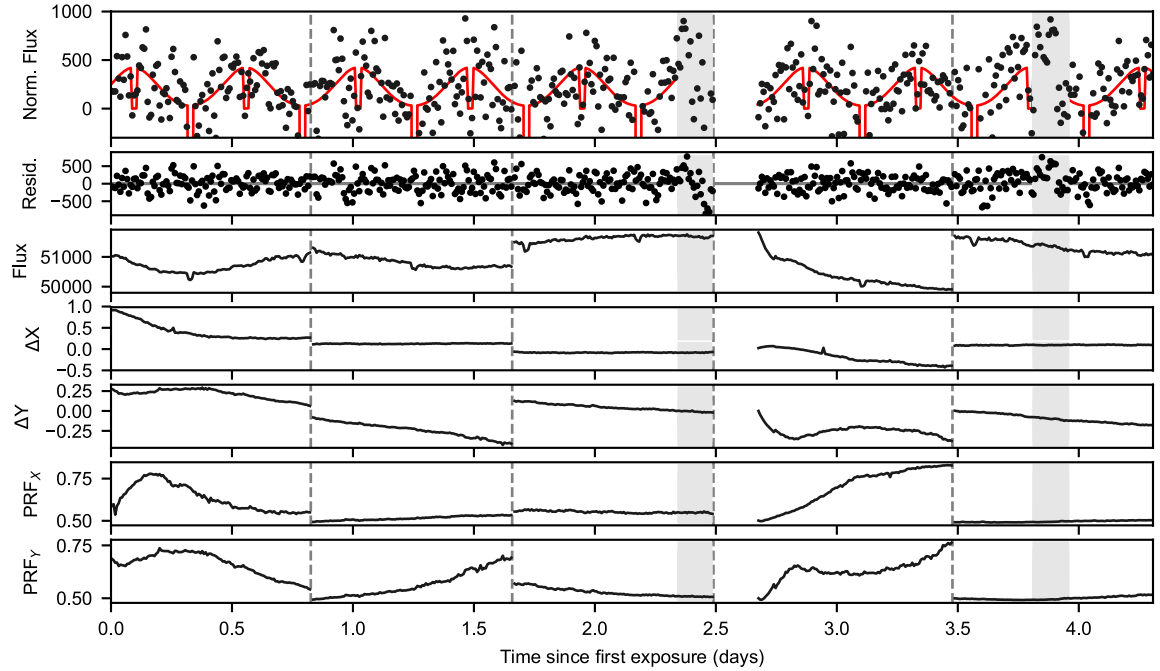

Extended Data Fig. 2 | LHS 3844b light curve and diagnostics. The top panel shows the normalized light curve ('Norm. Flux'; points) and best fit model (red line). The data are binned in 10-min increments. Regions marked in grey were masked in the fit because of time-correlated noise in the residuals. The second panel shows the residuals ('Resid.') to the best-fit model. The recorded flux in microjanskys is given in the third panel. The fourth and fifth panels from the top show the shift in X ('ΔX') and Y ('ΔY') of the target centroid on the detector. The two bottom panels show the width of the PRF in the X ('PRF$_X$') and Y ('PRF$_Y$') directions. Changes in telescope pointing are marked with dashed vertical lines. The gap after 2.5 days is due to the break for data downlink.

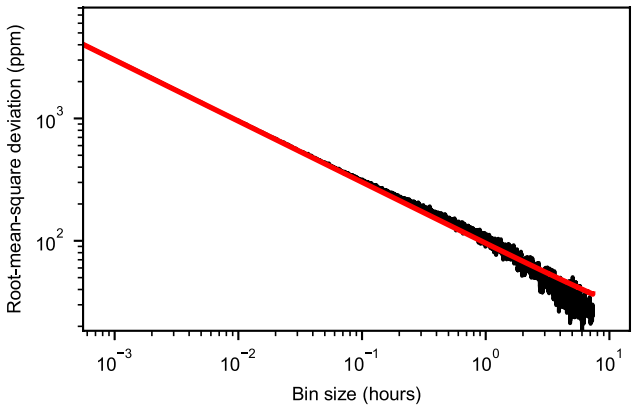

Extended Data Fig. 3 | Allan deviation for the residuals from the full fit of the phase curve. The data decrease as expected, with the photon noise on timescales from 2 s (one exposure) to 5.5 h (10^4 exposures).

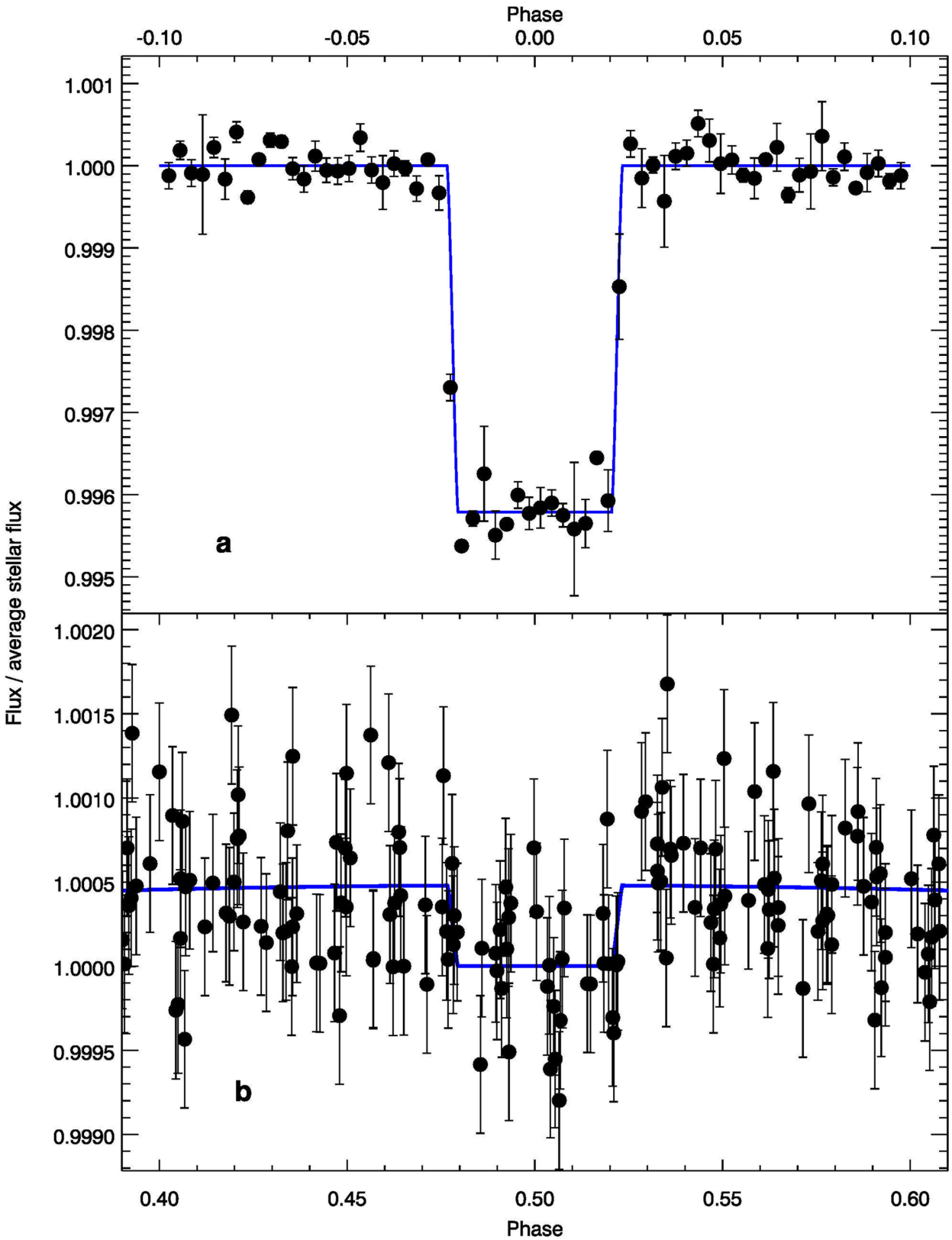

Extended Data Fig. 4 | Independent transit and eclipse fits. a, Spitzer transit of LHS 3844b at 4.5 μm, decorrelated using PLD (see text) and phased and binned for clarity. **b**, Spitzer secondary eclipse of LHS 3844b at 4.5 μm, decorrelated in a manner similar to the transit, but using a different binning. (The binning used in this figure is merely for illustration, and it is not the same as the binning used by our PLD code.) Blue lines represent the fits. The error bars correspond to 1σ uncertainties.

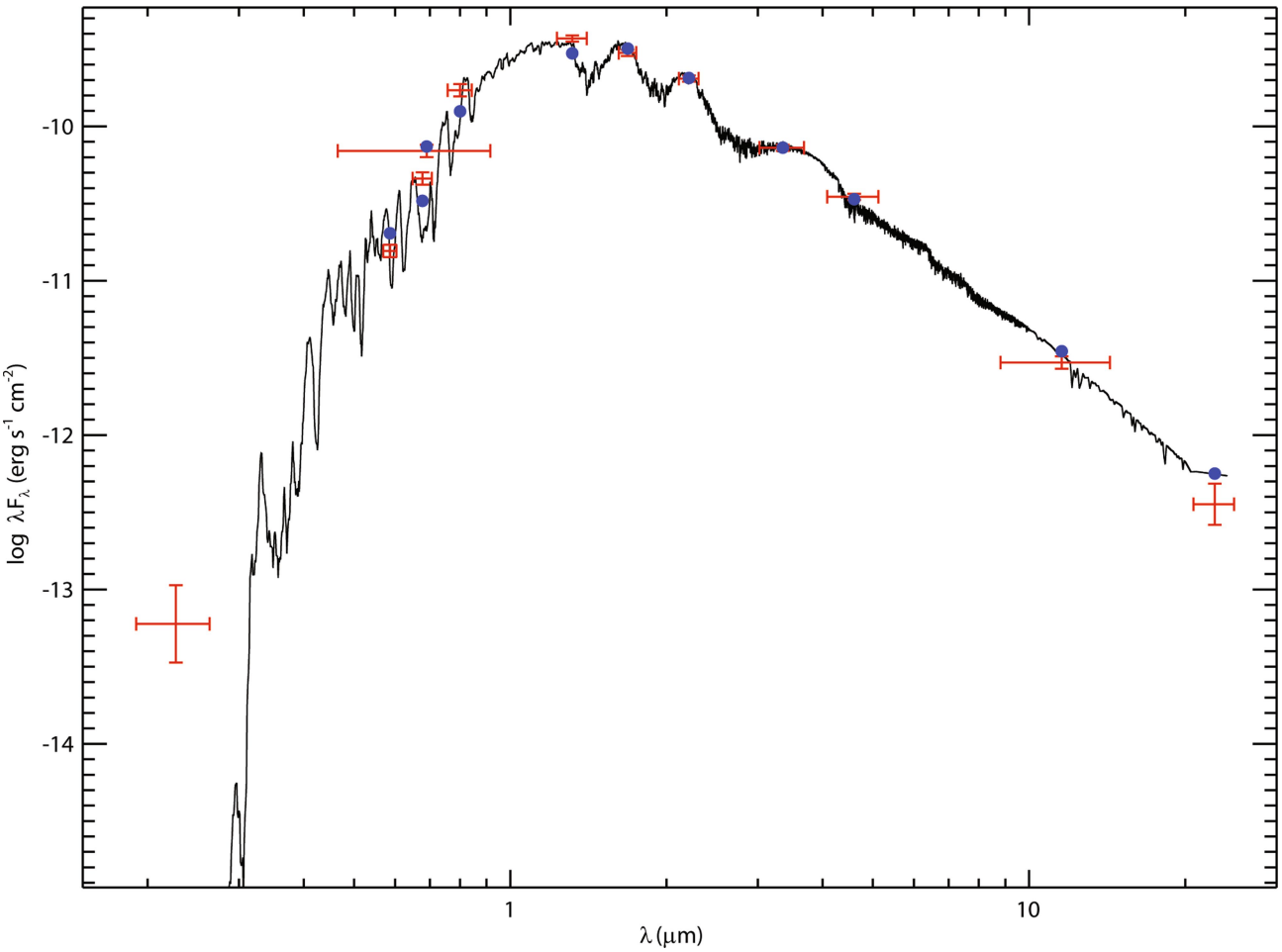

Extended Data Fig. 5 | Best-fit spectral energy distribution for LHS 3844. The red points are measurements, and the purple points represent the stellar model binned over each photometric bandpass. The vertical error bars represent 1σ uncertainties. The horizontal error bars represent photometric bandpasses.

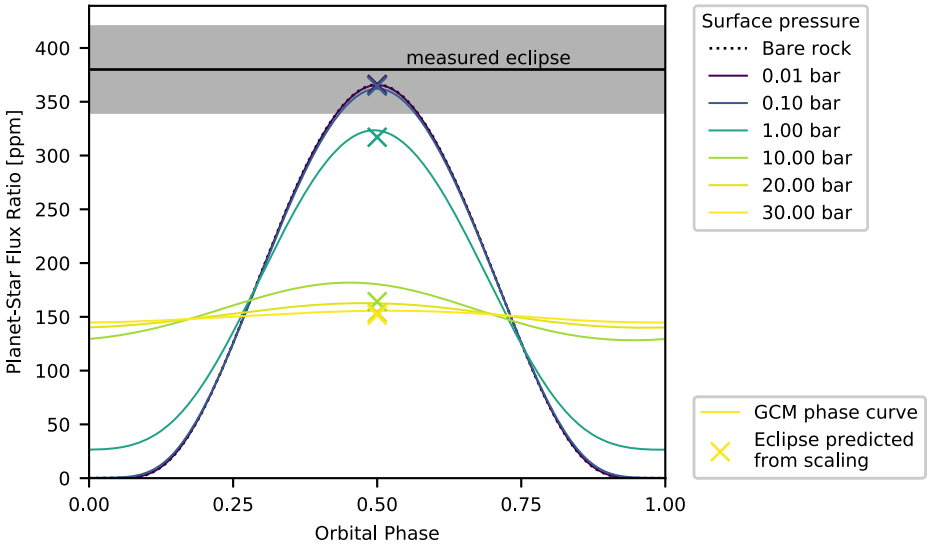

Extended Data Fig. 6 | Thermal phase curve of LHS 3844b in the Spitzer bandpass as a function of surface pressure, simulated with the GCM flexible modelling system[42–44]. We used semi-grey radiative transfer and increased the long-wave optical thickness linearly with surface pressure, $\tau_{LW} = p_s/(1\ \text{bar})$. The grey region shows the measured secondary eclipse with 1σ uncertainty, coloured lines show simulated phase curves and crosses show the dayside eclipses predicted by our analytic scaling. Thin atmospheres with surface pressure lower than 1 bar are indistinguishable from bare rock, whereas thick atmospheres become increasingly uniform.